Frequency conversion in two-dimensional photonic structure

Babic, L.

Chapter 3

Second harmonic generation in freestanding AlGaAs photonic crystal slabs

3.1 Introduction

Ever since the introduction as materials that can inhibit spontaneous emission [5] or localize light [6], photonic crystals have been recognized as structures that are able to tailor the propagation of light [9, 10]. These photonic crystals consist of a dielectric material arranged on a periodic lattice with a lattice constant comparable to the wavelength of light. Nowadays, photonic crystals find application in high Q, small mode volume cavities, in slow-light waveguides and numerous other applications that make use of the intriguing linear optical properties of photonic crystals. The nonlinear optics of photonic crystals, in particular second harmonic generation (SHG) is less intensively researched. Nevertheless, photonic crystals are interesting for nonlinear optics since they may combine high field intensities with optical properties that can be tuned by structure design.

In order to achieve highly efficient second harmonic generation in a small volume, a material with a large effective nonlinear susceptibility $\chi^{(2)}_{eff}$ must be used and the phase-matching condition must be met [29]. The phase-matching condition ensures that all waves generated inside the material interfere constructively. In most materials this condition is not fulfilled due to the material dispersion, but phase matching can be achieved using birefringent materials. The main obstacle in using III-V materials such as GaAs and GaP, that respectively have a more than 70 and 30 times larger $\chi^{(2)}_{eff}$ than that of a BBO crystal [31,32], is the fact that GaAs and GaP are not birefringent and phase-

matching is not easily satisfied. Phase matching can be satisfied in a device with periodically alternating layers of low and high index of refraction or by periodically poling the orientation of the $\chi^{(2)}$ material. An existing phase mismatch can be compensated by adding or subtracting a suitable reciprocal lattice vector $\mathbf{G}$ resulting in what is called quasi-phase-matching [33, 43–45]. Second harmonic generation can be further enhanced significantly by a strong spatial confinement of both the fundamental and the SH optical fields [46], that enhances the field intensities. Two-dimensional (2D) photonic crystal slabs, i.e., slabs of dielectric GaAs material perforated with a lattice of holes, are interesting in this respect.

Cowan et al. [47] show theoretically how to exploit the leaky modes of a freestanding 2D photonic crystal slab to achieve both quasi-phase-matching and strong spatial confinement. The authors predict an enhancement of SH signal in reflection of more than 6 orders of magnitude.

Mondia et al. [48] investigate experimentally SHG in reflection from a 2D square lattice of holes in GaAs supported on an Al_2O_3 cladding layer. The authors use very short (150 fs) pulses and vary the angle of incidence and the frequency of the fundamental beam. This enables them to make both the fundamental and the SH wave resonant with the leaky modes of the structure. In this quasi-phase-matched configuration they achieve a SH enhancement of more than 1200 times compared to the noise level in the experiment. Torres et al. [49] present a theoretical and experimental study of SHG in reflection from a 1D GaN photonic crystal. They report a SH enhancement of more than 5000 times, compared to an unpatterned GaN slab, when the quasi-phase-matching condition is satisfied.

We study in this chapter the influence of leaky modes at both the fundamental and SH frequency on SHG in reflection from a *freestanding* 2D photonic crystal slab, i.e., a slab that is surrounded by air on both sides. In principle, this would lead to a stronger confinement of the field and may therefore lead to more efficient SHG compared to earlier experiments. The photonic crystal consists of a regular 2D square array of holes drilled in ~ 150 nm thick slab of $Al_{0.35}Ga_{0.65}As$ material. Compared to earlier experiments in literature we use a narrow linewidth pulsed laser at 1.535 μm and tune the angle to probe the resonant coupling of both the fundamental and SH wave to the modes of the structure and how this affects the SH signal. We measure a SH enhancement of more than 4500 $\times$ compared to the signal from the photonic crystal away from resonance, and a SH enhancement of 35000 $\times$ relative to the second harmonic signal from the unpatterned $Al_{0.35}Ga_{0.65}As$ region on the wafer. These enhancements are significantly larger compared to enhancements

reported in References [48,49]. We measure our largest enhancement when the fundamental beam is slightly off-resonance. This shows the importance of the resonant coupling occurring at the SH frequency (quasi-phase-matching) and hints at the fact that the enhancement may be much larger in a structure that is doubly resonant.

3.2 Fabrication of photonic crystals

The photonic crystal samples, investigated in this chapter, consist of a free-standing slab perforated with a two-dimensional square lattice of holes. The starting point of the fabrication process, similar to that of Ref. [50], is the heterostructure shown in Fig. 3.1(a), grown along the <100> lattice direction of the GaAs crystal [51]. The purpose of the fabrication procedure is to create a large, freestanding slab made out of $Al_{0.35}Ga_{0.65}As$ perforated by a regular array of holes. A cross-section of this structure is shown in Fig. 3.1(b). The composition of the slab layer is chosen to render the structure optically transparent at both the fundamental (1535 nm) and second harmonic wavelength (767.5 nm).

The fabrication procedure starts with spin coating a $\sim$ 500 nm thick layer of a positive-tone e-beam resist, ZEP 520A [52], on top of the heterostructure. The two-dimensional square lattice of holes is defined in the resist using e-beam lithography. To ensure a nonzero efficiency for second harmonic generation, the ΓX direction of the photonic lattice is rotated relative to the crystallographic <100> direction of the underlying GaAs by an angle of $\sim 22.5°$. In this case, the incident electric field of the fundamental is never along a crystallographic axis of the GaAs wafer and the effective nonlinearity is nonzero. Collinear second harmonic generation along one of the crystallographic directions is forbidden due to the $4\bar{3}$m symmetry of the GaAs lattice.

After e-beam exposure, the exposed resist is removed by developing for 80 sec. in n-amyl acetate and rinsing for 30 sec. in 9:1 methyl isobutyl ketone:isopropyl alcohol solution. The developed resist then serves as an etch mask for transferring the pattern to the silicon nitride (SiN_x) layer using anisotropic reactive ion etching (RIE) in a CHF_3/Ar plasma. In this process a RF power of 50 W, a pressure of ~ 6 μbar and CHF_3 and Ar flow rates of 25 sccm are used. The etch rate of the SiN_x layer is $\sim$ 15 nm/min and the selectivity of the process is better then 10:1. After the pattern transfer, a low pressure RIE with an oxygen plasma is used to remove the residual e-beam resist.

Using the silicon nitride as a mask, the hole pattern is then etched deep

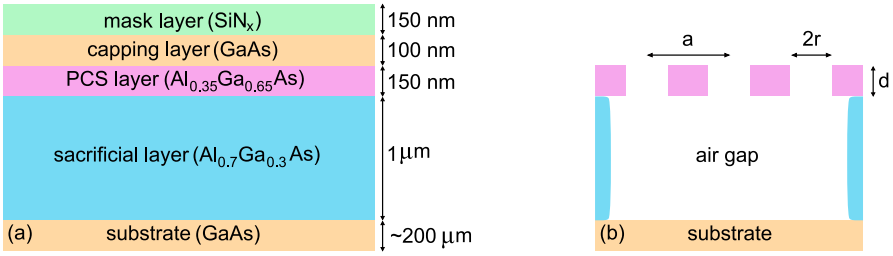

Figure 3.1. (a) Heterostructure used for fabrication of photonic crystal slabs. Photonic crystal slabs are made in the 150 nm thick $Al_{0.35}Ga_{0.65}As$ layer. The silicon nitride layer provides the mask for etching the hole pattern (defined by e-beam lithography) deep into the $GaAs/Al_xGa_{1-x}As$ layers. After removing the sacrificial layer a free-standing structure is achieved. (b) Schematic cross-section of a free-standing photonic crystal slab with lattice constant a, radius of the holes r and thickness d.

into the $GaAs/Al_xGa_{1-x}As$ layers in a chlorine-based RIE etch [53]. The flow rates of BCl_3, Cl_2, and N_2 are set to 15, 7.5, and 10 sccm, respectively. A pure chlorine plasma leads to isotropic etching of the GaAs. This can be compensated by adding a sufficient amount of nitrogen to the plasma to passivate the sidewalls during the etching process. This way, near vertical etch profiles can be realized, ensuring straight holes in photonic crystal layer [54]. The RF power and pressure are 100W and $\sim$ 4.5 μbar respectively and the selectivity of the process is better than 10:1. Afterwards, the remaining silicon nitride mask is removed using the CHF_3/Ar RIE as described earlier.

The 100 nm thick GaAs capping layer, on top of the structure, that protects the AlGaAs layers from oxidizing, is removed in a 3:1 citric acid:H_2O_2 solution* etch for 2 minutes [55]. The GaAs layer is etched $\sim$ 100 times faster then the underlying $Al_{0.35}Ga_{0.65}As$ layer. In order to obtain reproducible results, any oxide layer residing on top of the capping layer should be removed prior to the etching process by dipping the structure in 15:1 deionized H_2O:buffered oxide etch (BHF) solution for 15 seconds. Figure 3.2 shows a structure for which the removal of the GaAs is incomplete. The etching process is faster along the {100} crystallographic planes resulting in a square feature around every hole. From this image, the intentional $\sim$ 22.5° misalignment of the photonic and the crystal lattice of GaAs is clearly visible.

After removing the sacrificial $Al_{0.7}Ga_{0.3}As$ layer in a 1:4 HF (40%):H_2O

*The citric acid solution is made by mixing citric acid monohydrate with deionized water 1:1 by mass. The obtained solution is then mixed with a 31% H_2O_2 solution.

solution for 1 minute [50], critical point drying is used to remove the sample from the liquid, resulting in a freestanding photonic crystal slab. The samples for this chapter were fabricated using the facilities of the Kavli Nanolab Delft.

In this chapter, we investigate four freestanding photonic crystal slabs with the same lattice constant, but with a slightly different radius-to-pitch ratio r/a of the holes. These samples were created by writing the same pattern with e-beam using different exposures. Figure 3.3 shows an SEM image of sample D4 that was exposed with an electron dose of 250 μC/cm^2. From this image we find that the lattice constant $a = 890 \pm 2$ nm. An analysis of ~ 1000 holes shows

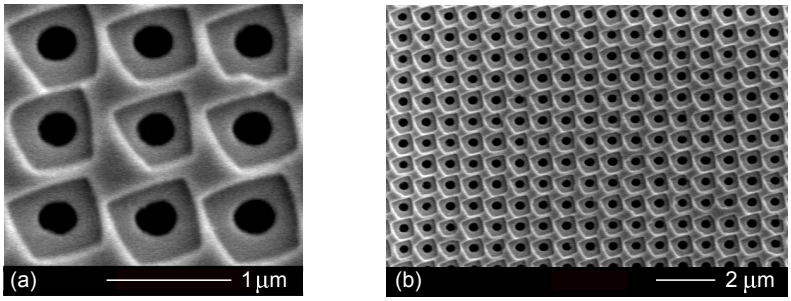

Figure 3.2. (a) and (b) SEM images of a photonic crystal sample with partially removed GaAs capping layer. Square feature around every hole arises from the fact that GaAs etches preferentially along the {100} crystallographic planes. The photonic lattice is rotated with respect to the crystal lattice of GaAs.

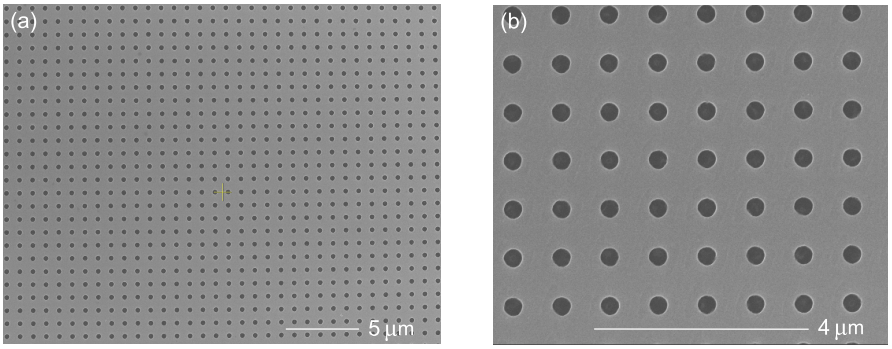

Figure 3.3. (a) and (b) Scanning electron micrographs showing the top view of freestanding photonic crystal slab D4. The entire structure covers an area of $\sim 300 \times 300$ μm^2. The radius of the holes is 160.9 nm, and the lattice constant is 890 nm.

that the radius of the holes is a normal distribution with an average radius of 160.9 nm and a standard deviation $\sigma = 1.6$ nm. The relevant parameters of photonic crystals D1–D4 are summarized in Table 3.1. As can be seen from the table, the hole size increases with electron dose. Varying the e-beam dose is a good way to fine tune the r/a ratio of a photonic crystal [56]. Samples D2, D3, and D4 have a similar distribution of hole sizes (equal σ) while D1 shows significantly more variation in hole size.

Table 3.1. Parameters of the photonic crystal slabs used in our experiments.

Sample label	**dose [μC/cm^2]**	a **[nm]**	r **[nm]**	**Area [μm^2]**
D1	220	890±2	144.1±3.2	$\sim 300 \times 300$
D2	230	-‖-	148.1±1.9	-‖-
D3	240	-‖-	154.6±2.0	-‖-
D4	250	-‖-	160.9±1.6	-‖-

3.3 Setup

The experimental setup used for both linear reflectivity and second harmonic generation is shown schematically in Fig. 3.4(a). All the measurements are done in a specular geometry where the angle of incidence θ_i is set by using a motorized stage.

3.3.1 Linear reflectivity

Two different white light sources are used to measure the linear reflectivity. A high power, fiber-coupled, Xenon lamp (Ocean Optics HPX-2000) is used in the infrared part of the spectrum ($\lambda \sim 900$–1700 nm) while a fiber-coupled Tungsten halogen lamp (Ocean Optics HL-2000-FHSA) is used at visible and near infrared wavelengths ($\lambda \sim 680$–900 nm). The advantage of the Tungsten over the Xenon lamp is that it has a flatter and more stable spectral output. The disadvantage of the Tungsten lamp is that it has less power in the infrared part of the spectrum. The white light coupled into a 50 μm multimode fiber (FIB.1) is collimated by lens L1 with a focal length of 50 mm. The collimated beam is then polarized by a Glan-Thompson polarizing beamsplitter cube (POL.) and focused on the sample by lens L2 with a focal length of 75 mm. Apertures AP.1 and AP.2 serve to modify the numerical apertures of both incident and collected beams. The reflected beam is collected and collimated

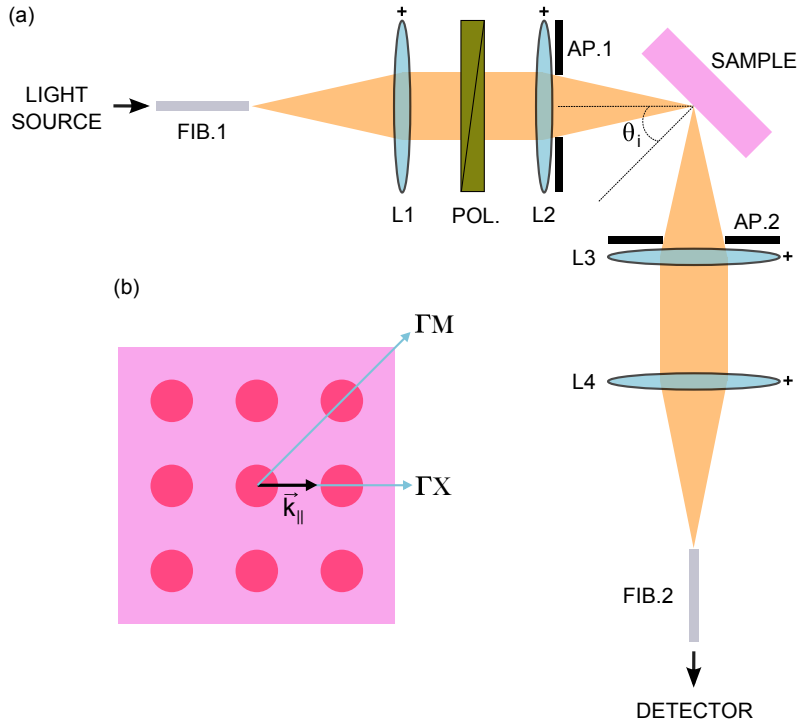

Figure 3.4. (a) Setup used for both linear reflectivity and second harmonic generation. Light from an illumination source is coupled into a fiber (FIB.1) and focused on the photonic crystal sample at an angle of incidence θ_i. The reflected light is collected into a second fiber (FIB.2) and sent to a detector. The lenses L1–L4 serve to collimate and focus the light onto the sample. A polarizer (POL.) adjusts the polarization of the incident light. The apertures AP.1 and AP.2 can be used to reduce the numerical aperture of the incident and collected beams. (b) Schematic top view of a square lattice photonic crystal slab. Relevant symmetry directions are indicated as well as the parallel component of the wave vector $\mathbf{k}_{||}$.

by lens L3 (focal length of 75 mm), and focused by lens L4 (focal length of 50 mm) onto a 400 μm multimode fiber (FIB.2) and then sent to a fiber-coupled grating spectrometer.

More than one spectrometer is employed in order to cover both visible and infrared part of the spectrum ($\lambda \sim$ 680–1700 nm). Ocean Optics USB2000 spectrometer (resolution $\approx$ 1.5 nm) is used for detection in the visible and near infrared part of the spectrum ($\lambda \sim$ 680–900 nm) while Ocean Optics

NIR-512 spectrometer (resolution $\approx$ 3nm) is used for the infrared part of the spectrum ($\lambda \sim$ 900–1700 nm).

3.3.2 Second harmonic generation

For SHG we slightly modify the setup shown in Figure 3.4(a). A Q-switched diode-pumped solid state laser (Cobolt Tango), with Er:Yb-doped glass as gain medium, is now used as the source of illumination. This laser has a specified center wavelength of 1535 ± 1 nm and a narrow linewidth, < 0.04 nm. The laser has a 5 kHz repetition rate with a typical pulse duration of ≈ 3.8 ns (full width at half maximum). The average power of the laser is ~ 25 mW and high peak power pulses (~ 1.3 kW) are generated. Light from the laser is coupled into a 9.5 μm single-mode fiber instead of the 50 μm multimode fiber used for linear reflectivity measurements.

The second harmonic generated in reflection is detected with either Ocean Optics USB4000 spectrometer (resolution $\approx$ 1.3 nm) or an Apogee Alta U1 Peltier cooled CCD camera. The CCD camera is used to detect very low second harmonic signals since it has much higher sensitivity compared to the fiber-coupled spectrometers.

3.4 Linear optical characteristics

The optical modes of a two-dimensional photonic crystal slab can be classified as truly guided modes and leaky modes (or guided resonances) [57]. Truly guided modes are the modes guided in the slab by total internal reflection. For these modes, all diffraction orders from the photonic crystal lattice are confined to the guiding layer as well. As a result, these modes remain confined to the slab and decay exponentially outside the slab. Leaky modes are the modes guided in the slab by total internal reflection that can couple to the environment via diffraction. In this case, at least one diffraction order from the photonic crystal lattice can propagate in the surrounding medium. Therefore, leaky modes can escape the slab and couple to the external radiation.

An effective way to investigate the leaky modes and their dispersion relation is to measure specular reflection spectra as a function of angle of incidence [58, 59]. Each guided resonance will appear as a resonant feature in the reflection spectrum on top of a slowly oscillating background [60]. Figure 3.5 shows a plot of the measured reflection for sample D4 as a function of frequency on the vertical axis and the in-plane wave vector $k_{||}$ on the horizontal axis. Data are shown for s-polarized (Fig. 3.5(a)) and p-polarized (Fig. 3.5(b)) light. In the experiment the angle of incidence θ_i is varied from 30° to 70° in

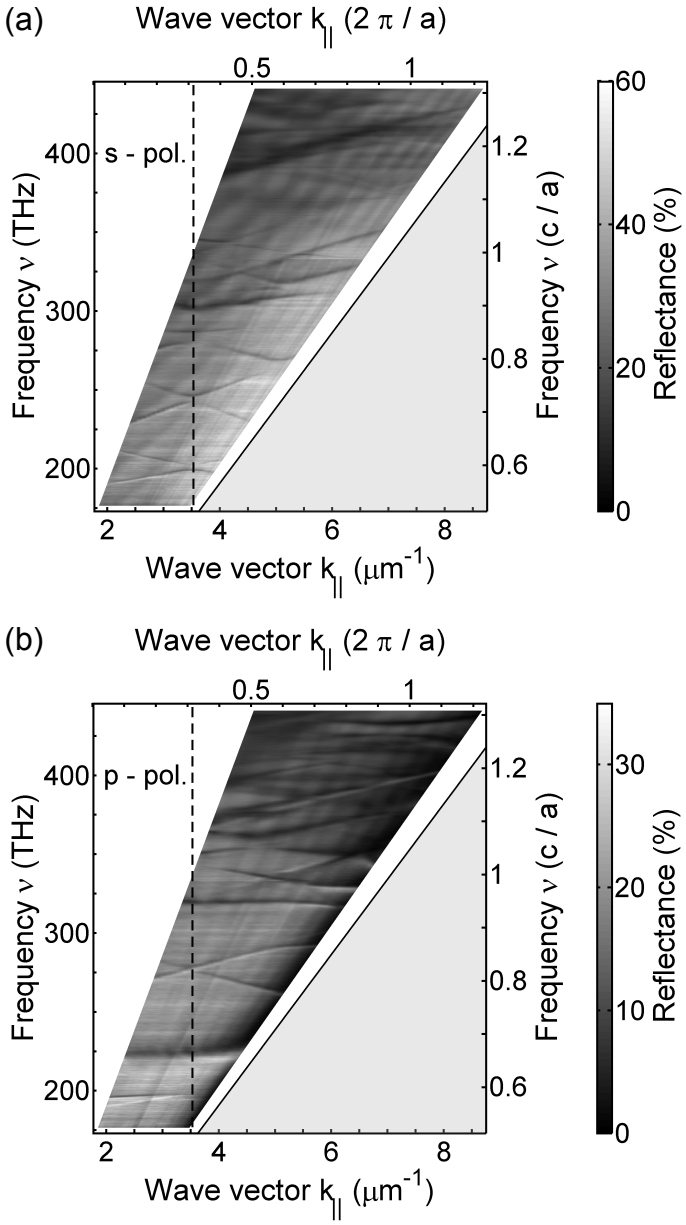

Figure 3.5. Gray scale plot of the measured reflection as a function of frequency (vertical axis) and wave vector $k_{||}$ (horizontal axis) for sample D4. Measurements are shown for s- (a) and p-polarized (b) incident light, and reveal the presence of several leaky modes. The gray shaded area below the light line (solid line) is where the truly guided modes exist.

steps of 1°. In order to facilitate a comparison with a dispersion relation $\nu(k_{||})$, the angles of incidence are converted to the in-plane wave vectors using the expression $k_{||} = (2\pi\nu/c)\sin\theta_i$, where θ_i are the angles of incidence, as shown in Figure 3.4(a). The sample is oriented in such a way that the in-plane wave vector, $\mathbf{k}_{||}$, is along the ΓX symmetry direction of the photonic crystal lattice. The incident light beam is focused to a spot of ~ 75 μm with a numerical aperture ~ 0.025. Several sharp resonant features can be observed in the figure indicating the dispersion of leaky modes. The gray shaded area below the light line ($\nu = ck_{||}/(2\pi)$) is the region of the truly guided modes.

In order to understand the position of the leaky modes, we calculated the band structure of the leaky modes using a freely available finite difference time domain (FDTD) package*. In the calculation, the slab has a radius of the holes $r/a = 0.18$, a thickness $d/a = 0.13$, and a relative permittivity $\epsilon = 10$. These parameters correspond to those of sample D4. For simplicity, we assume that the photonic crystal material is lossless and dispersionless and use a literature value [62] of the permittivity of $Al_{0.35}Ga_{0.65}As$ at a wavelength of 1500 nm. It is well-known that below the electronic band gap, the permittivity increases with frequency. Therefore, we expect that the calculated modes are slightly blue-shifted for larger frequencies compared to a calculation that takes into account dispersion. This is a relatively small effect in the frequency range where we compare the calculated band structure with measured data.

Figure 3.6 shows the calculated band structure of leaky modes plotted on top of the experimental reflectivity data for sample D4. We restrict ourselves to frequencies ν below 300 THz for clarity. Calculations are shown for both H-even (TE-like) and E-odd (TM-like) modes.

In the calculation, the 2D square lattice is positioned in the xy-plane and a point dipole source is placed in the middle of the photonic crystal slab at $z = 0$. The modes of a photonic crystal slab can be classified by their E-field, which is either *even* or *odd* with respect to the mirror-symmetry plane at $z = 0$. Even modes have the H-field in the z-direction, while odd modes have the E-field in the z-direction. In the case of an unpatterned waveguide slab, these modes correspond to the fundamental transverse electric (TE) and transverse magnetic (TM) modes. Note however, that this definition of TE and TM is relative to a plane of continuous translational symmetry, perpendicular to the slab; e.g., the $x = 0$ plane. This continuous translational symmetry is broken in a 2D photonic crystal slab and the optical modes cannot be labeled as TE and TM modes [63]. We will refer to these modes as a TE- and TM-like mode

*We use finite difference time domain package MEEP (MIT Electromagnetic Equation Propagation) [61], that can be found at http://ab-initio.mit.edu/wiki/index.php/.

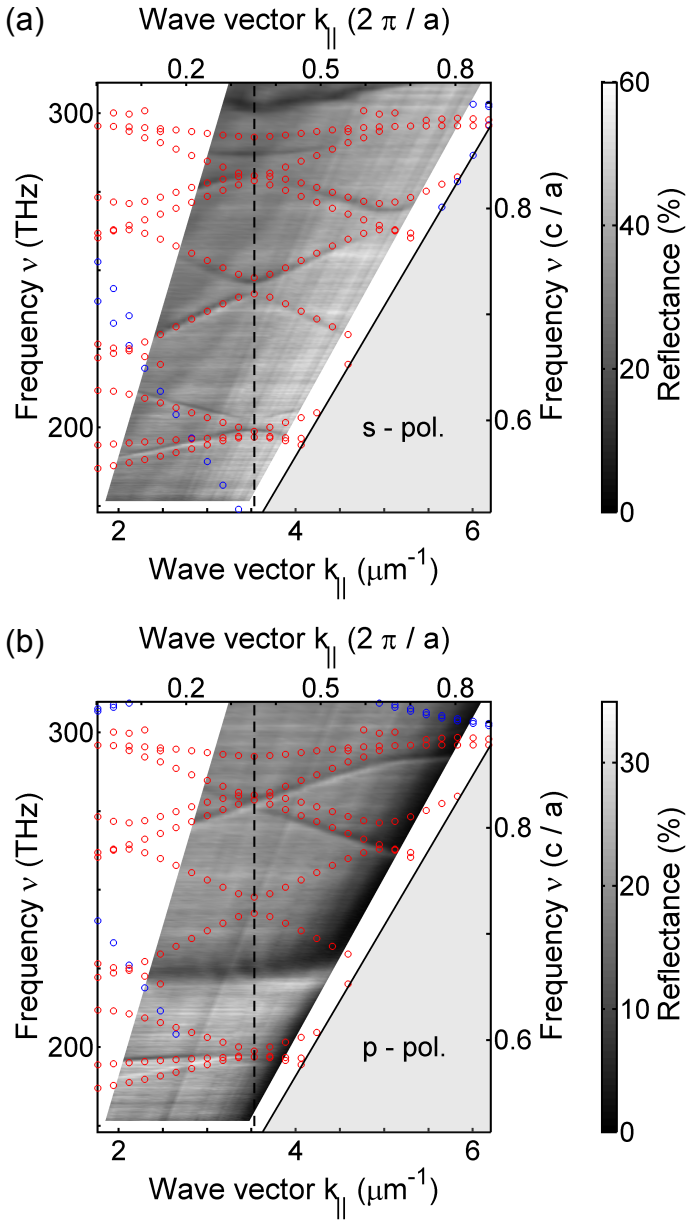

Figure 3.6. Calculated dispersion of leaky modes plotted on top of the experimental reflectivity data of Fig. 3.5 for s- (a) and p-polarized (b) light. The red and blue circles correspond to H-even (TE-like) and E-odd (TM-like) leaky modes, respectively.

to emphasize the resemblance of these modes to those of an unpatterned slab.

As can be seen, the calculated and the experimental data are in good agreement. From the figure we conclude that there is no coupling to TM-like leaky modes in this frequency range while a number of TE-like leaky modes are visible in the experimental data for both s- and p-polarized incoming light.

External radiation couples to the guided resonances of the photonic crystal via diffraction by adding a reciprocal lattice vector $\mathbf{G}$ to the in-plane wave vector $\mathbf{k}_{||}$. We define the wave vector of the incident light in the xz-plane, with the x-axis parallel to the ΓX direction of the photonic lattice. Each leaky mode can be labeled by the reciprocal lattice vector (G_x, G_y) involved in the coupling of the incoming light to the leaky mode.

In order to understand the coupling of the incident light to a leaky mode one needs to understand the symmetry of these modes in the plane of incidence. In our case, the plane of incidence is the $x = 0$ plane of mirror symmetry of the photonic crystal. The E-field of the leaky modes is either odd or even relative to this plane. Note that this definition of odd or even is an additional symmetry in addition to the mirror symmetry of the $z = 0$ plane discussed before. The E-field of the incoming s- or p-polarized light is either odd or even relative to the $x = 0$ plane. This determines the coupling of light to the slab modes.

Let us first consider the coupling to (±1, 0) and (0, ±1) modes. At non-normal incidence all degeneracy of these modes is lifted. The (-1, 0) and (+1, 0) modes show strong dispersion and propagate in the direction of the incoming wave vector. These TE-like modes are odd with respect to the $x = 0$ plane and couple to s-polarized light. The (0, ±1) modes propagate in and out of plane direction, and as a consequence have a weaker dispersion. The lower energy (0, ±1) mode is a superposition of a (0, +1) and (0, -1) mode with odd symmetry relative to the $x = 0$ plane and couples to s-polarization. The high energy (0, ±1) mode is even and couples to p-polarization [64]. This is indeed what is observed in Fig. 3.6. In the experimental data for s-polarization (Fig. 3.6(a)), going from low to high frequencies, we see a lower energy (0, ±1) mode, a (-1, ±1) mode, a crossing of (1, 0) and (-2, 0) modes, and a crossing of (1, ±1) and (-2, ±1) modes. The (-1, 0) mode is too low in frequency to be observed in the experiment. In p-polarization (Fig. 3.6(b)), we see a higher energy (0, ±1) mode, a (-1, ±1) mode with low Q (not resolved with MEEP calculation*), and a crossing of (1, ±1) and (-2, ±1) modes.

Sample D4 was designed in such a way to enable the coupling of a s-

*To eliminate the non-resonant contribution MEEP analyzes the field after a number of optical cycles. This excludes the contribution from modes with a low Q factor.

polarized fundamental beam at frequency $\nu_F = 195.44$ THz to one of the first leaky modes. From Figure 3.6(a), it is evident that the fundamental can resonantly couple to the structure by exciting the lower energy (0, ±1) mode. In order to determine for which value of the in-plane wave vector $k_{||}$ this is achieved we have to extract the dispersion of this leaky mode from the experimental reflectivity data.

Figure 3.7 shows reflection spectra of sample D4 for s-polarized incident light and various values of $k_{||}$. Each reflection spectrum contains sharp resonant features superimposed on top of a smooth background. The asymmetry of the (Fano) resonances is a result of an interference between a direct (non-resonant) and indirect (resonant) channel, as was first described by Fano [65, 66]. Light in the non-resonant channel is Fresnel reflected from the slab, while light in the resonant channel couples to a leaky mode of the structure and after some time "leaks" back into the environment. Fan et al. [60]

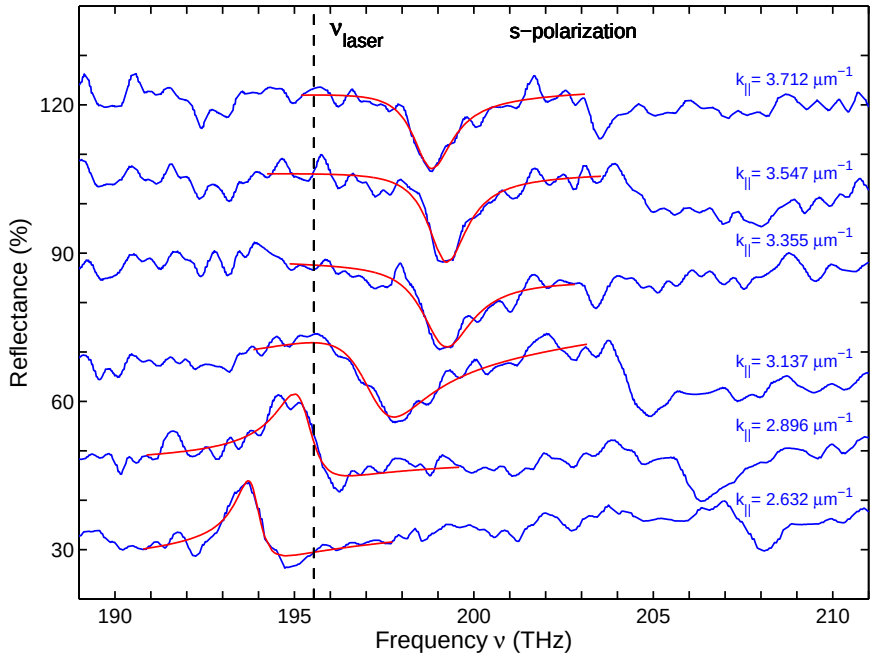

Figure 3.7. Experimental reflection spectra of sample D4 (blue curves) for s-polarized incident light and different values of $k_{||}$. Measured resonant features corresponding to the lower energy (0, ±1) leaky mode are well fitted with asymmetric Fano lineshapes (red curves). Black dashed line indicates the fundamental frequency.

have developed a general temporal coupled-mode theory of the Fano resonance for a single-mode optical resonator coupled with multiple input/output ports. A photonic crystal slab can be treated as a single-mode optical resonator with two ports, one at each side of the structure. Light, can be transported from one port to the other using both a non-resonant and a resonant channel. The resonant channel is characterized by a frequency ν_0 and a time τ. We define the escape rate of a resonance as $\Gamma = 1/(2\pi\tau)$ and the quality factor of a resonance as $Q = \nu_0/(2\Gamma)$. For a symmetric two port system, e.g., a freestanding photonic crystal slab in air, the reflectance R as a function of frequency ν is given by

$$R = \left| r_D + \Gamma \frac{-r_D \mp i t_D}{i(\nu - \nu_0) + \Gamma} \right|^2, \tag{3.1}$$

where r_D and t_D are the Fresnel reflection and transmission coefficients of the slab. The subscript "D" is used to denote the direct channel. The $\mp$ sign is due to exciting either *even* (-) or *odd* (+) leaky mode with respect to the plane of mirror-symmetry going through the middle of the slab ($z = 0$).

For a lossless system, the asymmetric Fano lineshape given by equation (3.1) reaches both 0% and 100%. In realistic systems, losses are present. These losses are either due to the absorption of the slab material or scattering from imperfections of the structure. Driessen et al. [67] have extended the coupled-mode theory of the Fano resonance by adding an extra port to include losses in the system. It is assumed that energy in the photonic crystal resonator is transferred irreversibly to the loss port and is characterized by a loss rate γ. The resonant Fano features in the experimental data, for a freestanding photonic crystal slab in air, can be described using the following expression for the reflectance R:

$$R = \left| r_D + \Gamma \frac{-r_D \mp i t_D}{i(\nu - \nu_0) + \Gamma + \gamma} \right|^2. \tag{3.2}$$

In order to fit the measured Fano resonances corresponding to the lower energy (0, $\pm$1) leaky mode (Fig. 3.7), the expression (3.2) is rewritten in the following form:

$$R = \left| c_1 + c_2\nu - \frac{c_3 + i c_4}{i(\nu - \nu_0) + \gamma + \Gamma} \right|^2, \tag{3.3}$$

where c_1, c_2, c_3, c_4, ν_0 and $\gamma + \Gamma$ are fit parameters. Here, we assume that the direct channel contribution to the total reflection, in the vicinity of a resonance, can be approximated with a linear function of the frequency ν. As can be seen from Fig. 3.7, the obtained fits show a good agreement with the experimental data. The importance of this approach is that we can extract the dispersion

(ν_0 as a function of $k_{||}$) and the quality factor ($Q = \nu_0/(2(\Gamma + \gamma))$ as a function of $k_{||}$) of a leaky mode directly from the experimental data. Figure 3.8 shows the dispersion of the lower energy (0, ±1) leaky mode of sample D4 (blue dots). The frequency of the fundamental is indicated by the red dashed line in the figure. The green dash-dot line defines a constant angle of incidence $\theta_i = 46°$. From this figure it is clear that the s-polarized fundamental beam couples resonantly to a leaky mode at an angle of incidence $\theta_i = 46°$, corresponding to $k_{||} = 0.417 \times 2\pi/a$. A typical quality factor $Q = \nu_0/(2(\Gamma + \gamma))$ of this leaky mode, as determined by the Fano model, is ~ 175.

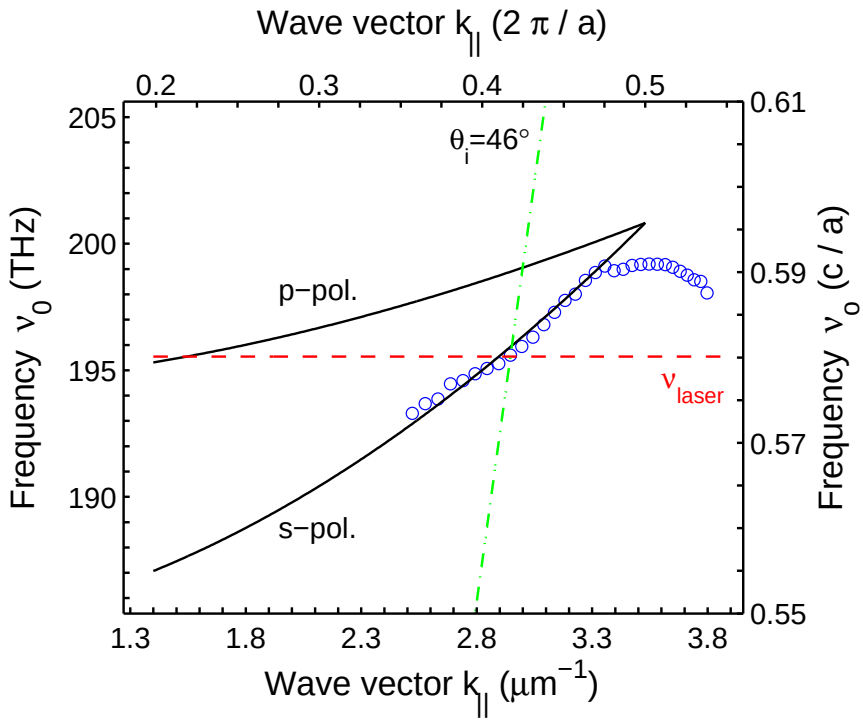

Figure 3.8. Measured dispersion of the lower energy (0, ±1) leaky mode of sample D4 (blue dots). The red dashed line indicates the position of the fundamental frequency, and the green dash-dot line corresponds to a constant angle of incidence $\theta_i = 46°$. Resonant coupling of the s-polarized fundamental beam to the (0, ±1) leaky mode occurs at an angle of incidence $\theta_i = 46°$. A simple analytical model, based on a nearly free photon picture (see text), is used to calculate the dispersion of both the lower and the higher energy (0, ±1) leaky mode (black curves).

A simple analytical model, that describes the dispersion (ν_0 as a function of $k_{||}$) of the (0, ±1) leaky modes, can be derived. In a nearly free photon picture, the light line of a uniform dielectric medium with an effective refractive index n_{eff} is folded back to the first Brillouin zone by adding an appropriate reciprocal lattice vector. For the hypothetical case of a slab with infinitely small holes, the (0, ±1) modes are degenerate. However, in a real photonic crystal slab, these modes split due to a standing wave pattern generated by the two counter-propagating (0, ±1) modes. The lower energy (0, ±1) mode has the maximum of the electric field in a high refractive index region, while the higher energy (0, ±1) mode has the maximum of the electric field in a low refractive index region. The dispersion of the (0, ±1) modes can be successfully approximated by only considering the interaction between the two (0, ±1) modes. The frequencies $\nu_{0\pm}$ of the modes are given by

$$\nu_{0\pm}(k_x) = \nu_c(k_x) \pm \Delta\nu(k_x)/2, \tag{3.4}$$

where ν_c is the center frequency, $\Delta\nu$ is the splitting between the modes, and k_x is the component of the incoming wave vector parallel to the interface in the ΓX direction. The center frequency $\nu_c(k_x)$ is given by

$$\nu_c = \frac{c}{2\pi n_{eff}} \cdot \left(\left(\frac{2\pi}{a} \right)^2 + \frac{1}{2} k_x^2 \right)^{1/2}, \tag{3.5}$$

and the splitting $\Delta\nu(k_x)$ between the two modes is given by:

$$\Delta\nu = \Delta\nu\,(k_x = 0) \cdot \left(\frac{a}{\pi} \right)^2 \cdot \left(\left(\frac{\pi}{a} \right)^2 - k_x^2 \right). \tag{3.6}$$

Here $\Delta\nu(k_x = 0)$ is the splitting at normal incidence that we obtain from the FDTD calculation. We find values of $n_{eff} = 2.52$ and $\Delta\nu(k_x = 0) = 0.029 \times$c/a.

3.5 Nonlinear optical properties

Figure 3.9 shows the measured power of the signal at a frequency of 390.88 THz (twice the fundamental frequency) as a function of the fundamental power (blue dots), generated in sample D4 and measured in reflection. A typical spectrum of the SH signal, measured with a fiber-coupled spectrometer, is shown in the inset. In order to achieve a dynamic range of ≈ 5 orders of magnitude, the detection scheme is changed by replacing the spectrometer with a silicon CCD camera. To make sure that we detect only the light at

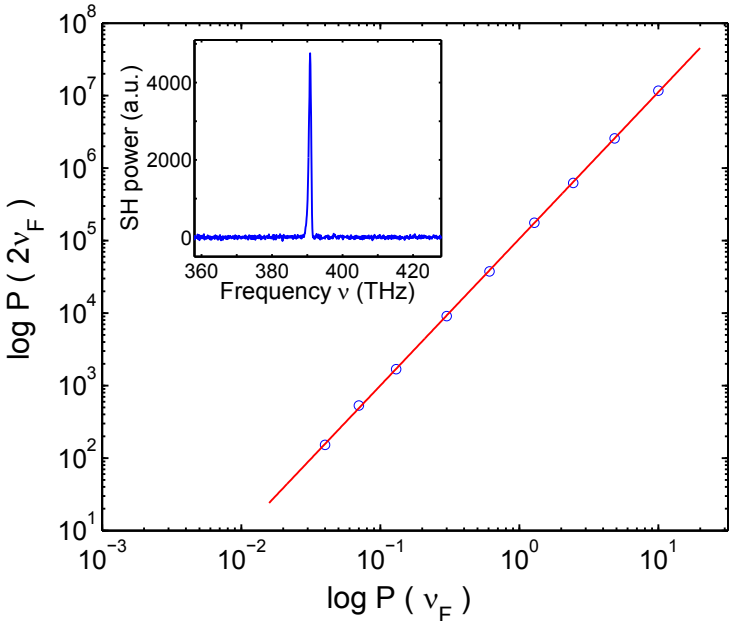

Figure 3.9. Measured power of the signal at a frequency of 390.88 THz as a function of the fundamental power (blue dots), generated in sample D4, and measured in reflection. The linear fit (red line) has a slope of 2.025 and confirms the quadratic power dependence. The inset shows a typical spectrum of the SH signal.

390.88 THz a bandpass filter with a center frequency of 391.17 THz and a full width at half maximum of 5.41 THz is placed in front of the CCD camera. The incident fundamental beam is clipped by an aperture and focused to a spot of ~ 35 μm with a numerical aperture of ~ 0.05. The power dependence measurement is done at a constant angle of incidence and polarization of the incident beam. As can be seen in the figure, the generated power at twice the fundamental frequency is proportional to the square of the fundamental power.

Figure 3.10 shows the second harmonic power (blue dots) generated by the s-polarized fundamental beam inside sample D4, as a function of the in-plane wave vector $k_{||}$. The in-plane wave vector $k_{||}$ is parallel to the ΓX symmetry direction of the photonic crystal lattice. The fundamental beam is clipped by an aperture and focused to a spot of ~ 75 μm with a numerical aperture ~ 0.025, and the second harmonic signal is detected using a fiber-coupled grating spectrometer. We varied the angle of incidence θ_i from 39° to 52°

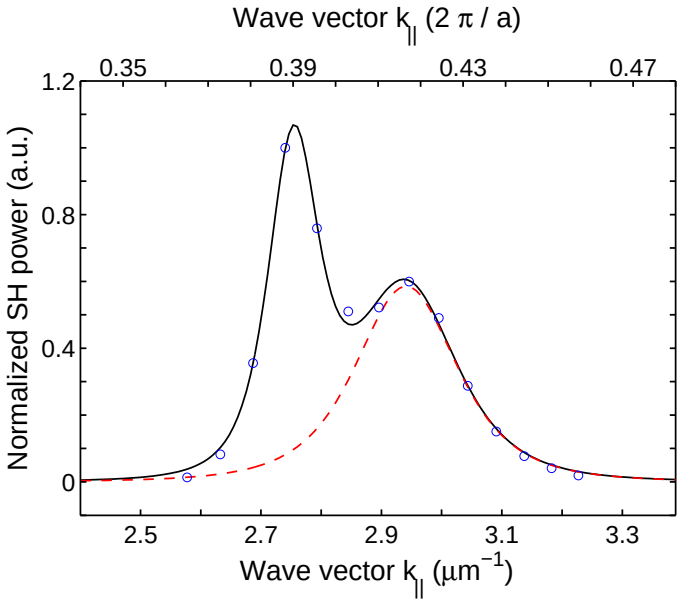

Figure 3.10. Second harmonic power (blue dots) generated by the s-polarized fundamental beam inside sample D4, and measured in reflection as a function of the in-plane wave vector $k_{||}$. Two distinct peaks in the SH power imply that two different resonant effects occur in the SHG. The measured SH power can be fitted with two Lorentzian-squared functions (black line). The red dashed line indicates the contribution to the SH due to a resonant coupling of the fundamental to the lower energy (0, ±1) leaky mode. The remaining contribution is due to a resonant coupling of the generated SH to a leaky mode of the structure.

in steps of 1° and converted this to the in-plane wave vectors $k_{||}$ using the expression $k_{||} = (2\pi\nu/c)\sin\theta_i$.

The measured second harmonic power for sample D4 shows two distinct peaks, implying that there are two different resonant effects that give rise to SH. The lower peak, occurring at $k_{||} = k_{||F} = 0.417\times 2\pi/a$, is due to the resonant coupling of the fundamental to the lower energy (0, ±1) leaky mode, as can be seen in Fig. 3.8. On resonance, we expect that the largest part of the fundamental power couples to the photonic crystal slab yielding the largest SH power. The power at the fundamental frequency ν_F inside the slab is given by

$$P_{in\ slab}(\nu_F, k_{||}) \propto \frac{\Gamma(k_{||})^2}{(\nu_F - \nu_0(k_{||}))^2 + (\Gamma(k_{||}) + \gamma(k_{||}))^2}, \tag{3.7}$$

where ν_0, Γ and γ are the center frequency, escape and loss rates of the lower energy (0, $\pm$1) leaky mode respectively. Assuming that the parameters Γ and γ are slowly varying functions of $k_{||}$ for the range of in-plane wave vectors used in the SHG experiment, expression (3.7) becomes:

$$P_{in\ slab}(\nu_F, k_{||}) \propto \frac{1}{(\nu_F - \nu_0(k_{||}))^2 + (\Gamma + \gamma)^2}. \tag{3.8}$$

Since the center frequency ν_0 can be approximated well with a linear function of $k_{||}$ for the range of in-plane wave vectors used in the SHG experiment (Fig. 3.8), we rewrite expression (3.8) as:

$$P_{in\ slab}(\nu_F, k_{||}) \propto \frac{1}{(k_{||F} - k_{||})^2 + \left(\frac{\Delta_F}{2}\right)^2}. \tag{3.9}$$

Thus, the fundamental power inside the photonic crystal slab as a function of $k_{||}$, can be described with a Lorentzian function peaked at $k_{||F}$ with a full width at half maximum (FWHM) Δ_F. The position of the peak, $k_{||F}$, is determined by the dispersion of the leaky mode, and the width of the Lorentzian, Δ_F, is determined by the quality factor of the mode. For the second harmonic power generated in the photonic crystal we write:

$$P_{in\ slab}(2\nu_F, k_{||}) \propto \left(\frac{1}{(k_{||F} - k_{||})^2 + \left(\frac{\Delta_F}{2}\right)^2} \right)^2. \tag{3.10}$$

The measured SH power can be fitted with two Lorentzian-squared functions of the form (3.10), as shown by the black line in Fig. 3.10. The peaks are positioned at $k_{||SH} = 0.390\times 2\pi/a$ and $k_{||F} = 0.417\times 2\pi/a$, and have a width $\Delta_{SH} = 0.011\times 2\pi/a$ and $\Delta_F = 0.022\times 2\pi/a$. The dashed red line in Figure 3.10 shows the contribution to the SH due to the resonant coupling of the fundamental to the lower energy (0, $\pm$1) leaky mode at $k_{||} = 0.417\times 2\pi/a$.

The remaining contribution to the SH cannot be explained by considering only the resonance at the fundamental frequency. The fundamental beam is off-resonance at $k_{||} = 0.390\times 2\pi/a$ (Fig. 3.8), where we measure the highest SH signal. We suggest that there is a contribution to the SH signal due to the resonant coupling of the generated wave at the second harmonic frequency to one of the leaky modes of the photonic crystal slab. Unfortunately, we are not able to identify a specific leaky mode in either the reflectivity measurements or in the MEEP calculation. At higher frequencies, the band structure becomes very complex due to the large number of bands involved and strong

interaction between them. In fact, a measurement of second harmonic using a tunable laser might be a better way to characterize the leaky modes at higher frequencies.

Figure 3.11 shows a comparison of the nonlinear optical response of samples with slightly different radius-to-pitch ratio r/a of the holes. The SH signal is measured in reflection as a function of the in-plane wave vector $k_{||}$ for samples D1 (pink), D2 (green), and D3 (blue dots). The curves are offset vertically by a constant value for clarity. The experimental data for sample D4 (red dots), as discussed earlier, are shown in the figure as well.

We observe that the second harmonic signal shifts to larger values of $k_{||}$ as the ratio r/a decreases. This effect can be understood by considering a nearly free photon picture. In this picture, a decrease in the ratio r/a results in an increase of the effective refractive index of the slab (n_{slab}) and shifts the dispersion of the leaky mode ($\nu \propto k_{||}/n_{slab}$) towards lower frequencies. As a consequence, the fundamental beam becomes resonant with the photonic crystal at a larger value of the in-plane wave vector $k_{||}$. The black arrows in the figure indicate the values of $k_{||}$, estimated from experimental linear reflectivity data, for which the fundamental beam is exactly on resonance.

As can be seen from the figure, the signals from samples D1 and D2 are very comparable. This is due to the fact that these samples have the same pitch and almost equal hole size. The main difference between the samples is that sample D1 has a larger variation in the hole size compared to other samples (Table 3.1).

For all samples, the SH is generated over a relatively large range of $k_{||}$ and cannot be explained by considering only the coupling of the fundamental beam to the structure. It is clear from the dispersion of the lower energy (0, $\pm$1) leaky mode that the fundamental beam is "far away" from being exactly on resonance with either sample D1 or D2 in the region around $k_{||} = 0.5{\times}2\pi/a$. We believe, that resonant effects at second harmonic frequency provide an answer. Note that for these values of $k_{||}$ the leaky mode at the SH frequency is close to the edge of the first Brillouin zone, as indicated by the black vertical dash-dotted line in Fig. 3.11. Since the group velocity vanishes at the edge of the Brillouin zone, coupling to such a mode could lead to a very broad feature in the measured SH.

As a final note, we emphasize the presence of a peak in the SH signal occurring in the second Brillouin zone. To visualize this peak, we multiply the SH power generated in sample D4 for larger values of $k_{||}$, by a factor of 10. A weak peak occurs at $k_{||} \approx 0.57{\times}2\pi/a$ due to a higher order diffraction of the periodic lattice at the fundamental frequency. The magnitude of this peak is

much lower since the higher order diffraction event is less efficient.

The calculated enhancement of the SH signal for a similar geometry was found to be more than 6 orders of magnitude [47]. In order to estimate the SH enhancement for sample D4, we measured both the resonant and the non-resonant contribution to the SH signal generated in the sample, and calculated the ratio. The non-resonant contribution can be measured by tuning the $k_{||}$ in such a way that the waves at both the fundamental and the second harmonic frequency cannot resonantly couple to the structure. We are limited by the

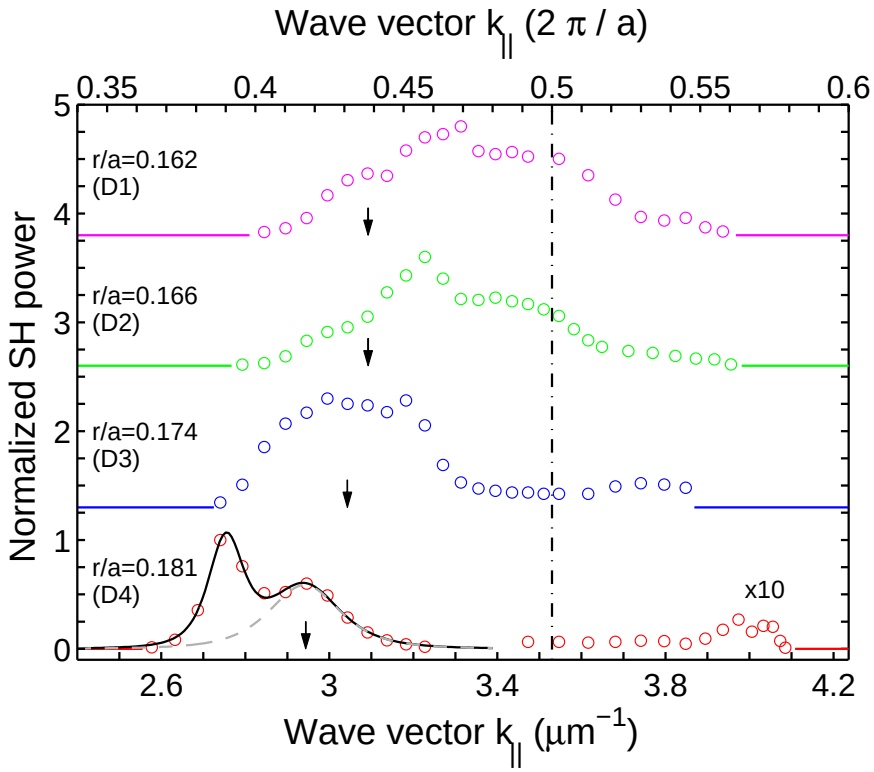

Figure 3.11. Second harmonic power measured in reflection as a function of the in-plane wave vector $k_{||}$ for samples D1 (pink), D2 (green), D3 (blue), and D4 (red dots). The curves are offset by a constant value for clarity. The black arrows indicate the values of $k_{||}$ for which the fundamental beam is exactly on resonance with the given structure. The vertical dash-dotted black line indicates the position of the edge of the first Brillouin zone. As the ratio r/a decreases, the SH signal shifts to the larger $k_{||}$.

noise floor of the spectrometer in measuring this contribution, and estimate a lower limit of the SH enhancement for sample D4 of 4500, which is almost 4 times larger than the maximal enhancement reported in Reference [48]. The maximal SH signal generated in reflection from sample D4 occurs at $k_{||}$ for which the fundamental is slightly off-resonance, as can be seen in Figure 3.10. This implies that even larger enhancements can be achieved for a structure that enables the resonant coupling at both the fundamental and SH frequency at the same time. Based on the fit with two Lorentzian-squared functions in Fig. 3.10, we estimate that the signal may be further enhanced by a factor of 10. We also compared the resonant SH generated in reflection from the sample to the SH generated in reflection from the unpatterned $Al_{0.35}Ga_{0.65}As$ region on the wafer. A detection scheme with a very sensitive silicon CCD camera, described earlier, is used to detect low SH signal generated from the unpatterned region. The highest measured second harmonic signal from the photonic crystal slab is $9225 \pm 3 \times 10^3$ cts/s. The measured second harmonic signal from the unpatterned region is $0.26 \pm 0.03 \times 10^3$ cts/s. Therefore, the experimental SH enhancement is $35 \pm 4 \times 10^3$ times, which is 7 times larger than the enhancement reported in Reference [49] for 1D GaN structures.

3.6 Conclusion

Leaky modes at both the fundamental and the SH frequency play a prominent role in increasing the nonlinear optical response of a photonic crystal slab. By tuning the in-plane wave vector $k_{||}$ of the incident fundamental beam the structure can be resonantly excited, leading to large enhancements of second harmonic. We measure an enhancement > 4500 when compared to the photonic crystal slab off-resonance, and a factor 35000 compared to an unpatterned substrate.

The observation of two distinct peaks in the SH signal generated in sample D4 can be explained with the resonant coupling at both the fundamental and the SH frequency. In fact, the largest SH enhancement for sample D4 occurs when the fundamental beam is slightly off-resonance, and we estimate that the SH can be enhanced by another factor 10. To investigate the enhancement in more detail, a better understanding of the leaky modes at the SH frequency is needed. An interesting new route to investigate the influence of the modes at the SH frequency on the SHG would be to design and make a photonic crystal slab that has one of the first leaky modes at the SH frequency. In this way, the coupling of the fundamental to the structure can be neglected and all the features in the SH signal can be attributed to resonant effects at SH

frequency.